Journal of King Saud University – Science 32 (2020) 2059–2068

Contents lists available at ScienceDirect

Journal of King Saud University – Science

journal homepage: www.sciencedirect.com

Original article

Synthesis, characterization, and selective benzyl alcohol aerobic oxidation over Ni-loaded $BaFeO_3$ mesoporous catalyst

Naushad Ahmad [a,*], Manawwer Alam [a], Syed Farooq Adil [a,*], Anees A. Ansari [b], Mohamed E. Assal [a], Shahid M. Ramay [c], Mukhtar Ahmed [d], M. Mujahid Alam [a], Mohammed Rafiq H. Siddiqui [a]

[a] *Department of Chemistry, King Saud University, Riyadh 11451, Saudi Arabia*
[b] *King Abdullah Institute for Nanotechnology, King Saud University, Riyadh 11451, Saudi Arabia*
[c] *Department of Physics, King Saud University, Riyadh 11451, Saudi Arabia*
[d] *Department of Zoology, King Saud University, Riyadh 11451, Saudi Arabia*

ARTICLE INFO

Article history:
Received 27 September 2019
Revised 24 December 2019
Accepted 10 February 2020
Available online 19 February 2020

Keywords:
Perovskite
Surface area
Molecular oxygen
Benzyl alcohol
Catalytic oxidation

ABSTRACT

A series of cubic porous perovskites with the general formula $BaFe_{1-x}Ni_xO_3$ have been prepared via the sol-gel-citrate route and investigated as a catalyst for the aerobic oxidation of benzyl alcohol (BzOH) to benzaldehyde (BzH) using molecular O_2 as the oxidant under ambient pressure. Doping and the synergetic interaction between Ni and Fe ions in the $BaFeO_3$ perovskites significantly affected the conversion, product selectivity, specific activity, turnover number, and turnover frequency. A BzH selectivity of >99.9% was achieved in the oxidation of BzOH. Among the prepared perovskites, $BaFe_{0.4}Ni_{0.6}O_3$ showed the highest catalytic conversion and specific activity under the optimized reaction conditions. Based on the catalytic performance, further studies on the recyclability, and influences of temperature and catalyst loading were carried out using this catalyst. The catalyst recyclability test showed a negligible loss in activity after five consecutive cycles.

1. Introduction

The catalytic oxidation of BzOH has received tremendous attention in current green and chemical process research. Careful designing to develop a robust catalyst with a superior activity and/or selectivity for controlled BzOH oxidation to aldehydes or ketones is a core task to preclude further transformation to undesirable products (Ferguson and Ajjou, 2003; Peyrovi et al., 2005; Sheldon et al., 2000; Su et al., 2008). Many oxidants such as *tert*-butyl hydroperoxide, hydrogen peroxide, chromium trioxide, and ammonium permanganate have been utilized to achieve this oxidation. However, these oxidants have serious drawbacks such as high cost, toxicity, corrosiveness, and the requirement of severe conditions for the oxidation process (Luo et al., 2014). Based on the environmental and economic aspects of BzH production, many efforts have been devoted to the design of cost-effective recycling catalytic oxidation reactions with regard to the preservation of natural oil resources, using molecular oxygen as a clean oxidant because it is readily available and produces water as the byproduct (Mallat and Baiker, 2004; Sawayama et al., 2006; Yamamoto et al., 2005). In this context, there are a large number of reports on oxidation using noble metals (e.g., Pd, Pt, Ru, Au, and Ag) as the efficient heterogeneous catalysts with superior activity and selectivity (Choudhary et al., 2005; Enache et al., 2006; Opre et al., 2006; Zhan and Thompson, 2004; Zhan et al., 2012). Nevertheless, the rising cost and rareness of these metals are restricting their utilization. Researchers are investigating the use of various types of inexpensive transition metals (Mn, Fe, Ni, and Cu-based catalysts) that are comparable with noble metal catalysts in terms of their selectivity, reusability, and catalytic activity. Less expensive metals are cost-effective alternatives to noble metal catalysts, and their low catalytic activity may provide more insight into the reaction mechanism (Yang et al., 2010; Zhu et al., 2010).

In addition to noble- and transition-metal-based catalysts, perovskite materials (ABO_3) have gained much attention due to their low cost and because they enable environmentally controlled reaction systems that effectively adopt a recyclable catalyst and clean molecular oxygen (Attaoua et al., 2012; Haruna et al., 2019;

---

* Corresponding authors.
E-mail addresses: anaushad@ksu.edu.sa (N. Ahmad), sfadil@ksu.edu.sa (S.F. Adil).

Peer review under responsibility of King Saud University.

Production and hosting by Elsevier

https://doi.org/10.1016/j.jksus.2020.02.015
1018-3647/

Liu et al., 2014; Zang et al., 2019). Perovskites with flexibility of the A-site and/or B-site have received tremendous interest owing to their various industrial applications such as catalysis, combustion processes, photo-electrochemistry, solid oxide fuel cells, gas sensors, humidity sensors, emission control superconductors, and battery electrodes (Alifanti et al., 2003; Berger et al., 2007; Ghasdi et al., 2011; Karimi et al., 2014; Merino et al., 2005; Pena and Fierro, 2001; Royer et al., 2005). The catalytic performance of perovskites mainly depends on the nature of the B-site metals (Abdolrahmani et al., 2010; Gallagher et al., 1977). Many investigations have been carried out to change their catalytic activity and stability behavior via partial substitution of the A and/or B cations with cations of different sizes (Forni et al., 1996; Islam et al., 2018; Ma et al., 2014; Madduluri et al., 2019; Mitran et al., 2019; Szabo et al., 2003; Zhang-Steenwinkel et al., 2002). One of most typical perovskite oxides, A-FeO_3, has been intensively investigated over the last few years due to its potential catalytic activity (Zheng et al., 2000). The introduction of a small fraction of other active metals significantly improved the stability and activity of the derived materials (Pan et al., 2015). A-Fe-NiO_3-type perovskites catalyze a broad range of conversion reactions and are exemplary catalysts for the elimination of organic dyes in oxidative-condition media due to their outstanding hydrothermal stability, controllable oxygen vacancies, and capability to inclusion several metal ions without destruction of the matrix lattice (Hashemian and Foroghimoqhadam, 2014; Royer et al., 2014). Fe ions, which are the main components of conventional Fenton catalysts, can be existed in perovskite frameworks such as $LaFeO_3$, and utilized as heterogeneous catalysts for RhB oxidation (Xiao et al., 2013).

Several methods have been used for the preparation of low-cost perovskites that exhibit a range of catalytic performances; they are broadly classified as solid–solid reactions and liquid–solid reactions. Sol–gel citric chemical (SGC) routes for the synthesis of perovskites have attracted considerable attention for years because they are very effective in controlling the B-cation ordering degree and microstructure, purity, and homogeneity of the end product (Arakawa et al., 1985). In this study, a series of nickel-doped $BaFeO_3$ perovskites was synthesized using an SGC method and the catalytic activity for aerial oxidation of BzOH was tested in presence of O_2. The fabricated catalysts were characterized using XRD, ICP, FT-IR, SEM, TEM, TGA, BET, and temperature-programmed reactions (e.g., H_2-TPR, O_2-TPO, and CO_2-TPD) to reveal the synergistic interactions between the Fe and Ni domains and the relationship between the composition/structure of the catalyst and catalytic efficiency.

2. Experimental

2.1. Catalyst synthesis

$Ba(NO_3)_3$ $6H_2O$ (Alfa Aesar, 99.5%), $Ni(NO_3)_2$ $6H_2O$ (E-Merck, 99.5%), $Fe(NO_3)_3{\cdot}9H_2O$ (E-Merck, 99.5%), and citric acid monohydrate (E-Merck, 99.5%) were utilized without any further purification. $BaFe_{1-x}Ni_xO_3$ (x = 0.0, 0.2, 0.4, 0.6, and 0.8) catalysts were prepared via sol–gel–citrate procedure (Escalona et al., 2010). In this synthesis, appropriate quantities of $Ni(NO_3)_3$ $6H_2O$, $Fe(NO_3)_3$ $6H_2O$, $Ba(NO_3)_3$ $6H_2O$, and citric acid were separately dissolved in deionized water until the formation of a limpid solution. After dissolution, the metal nitrate solutions were mixed and agitated for about 30 min. A concentrated solution of citric acid was thereafter added in 10 wt% excess over the stoichiometric quantity to ensure the complexation of metal ions. The resulting solution was stirred for 2 h at 80 °C and evaporated at 120 °C on a rotary evaporator until gel formation. The resulting gel was dried overnight in a vacuum oven set at 250 °C, and calcined in air at 800 °C for 6 h to prepare perovskite crystals. The calcination condition was selected based on the thermal analyses of the precursors.

2.2. Catalyst characterization

The as-prepared catalysts were analyzed using various characterization instruments and all experimental details are given in supplementary file.

2.3. Catalytic studies

The aerobic oxidation reaction of BzOH was performed at atmospheric pressure in a three-necked glass flask equipped with condenser and thermometer, as mentioned in reference (Assal et al., 2019). In brief, 200 mg catalytic agent, 2 mmol BzOH, and 10 mL toluene (solvent) were transferred into a 50 mL flask. Prior to the oxidation process, the reaction mixture was purged using Ar gas for 1 h. The mixture was immersed in an oil bath and heated to 100 °C. Oxygen gas was bubbled into the pre-charged flask at a rate of 20 mL min^{-1} to start the reaction. The liquid products were collected every 2 h and analyzed using an Agilent gas chromatograph 7890A equipped with an FID and a HP-PONA capillary column. The conversion of BzOH and the selectivity towards BzH were calculated using the peak area. The effects of the amount of catalyst, reaction time, temperature, and recycling were investigated.

3. Results and discussion

3.1. Chemical composition

The metal contents of the $BaFe_{1-x}Ni_xO_3$ perovskites are compiled in Table 1. A close similarity between the nominal and analytical values was found in each case, indicating the efficiency of the catalyst preparation method. Nevertheless, oxygen deficiencies were present in the synthesized perovskites.

The chemical compositions of the prepared precursors, determined using FT-IR spectroscopy, are depicted in Fig. 1. The prepared precursors exhibit nearly the same compositional spectra. The broad peak band between 3200 and 3450 cm^{-1} in the spectra is assigned to the stretching vibration of physically adsorbed water (O—H) molecules. The band appearing at 2905 cm^{-1} is due to atmospheric CO_2 adsorbed during pellet preparation (Thirumalairajan et al., 2014). The symmetric and asymmetric stretching vibrations of the carboxyl group appear at 2357 and 1464 cm^{-1}, respectively. The N—O of the nitrate group and H—O—H planar water bands appear at 1387 and 1615 cm^{-1}, respectively (Gajbhiye et al., 1995; Ponce et al., 2000). The less intense band noted at 1018 cm^{-1} corresponds to the vibration of the CO_3^{2-} group, signifying that Ba-carbonate exist on the surface of the precursors. The spectra show bands at 617 and 459 cm^{-1}, which are characteristic of mixed metal oxides although they are shifted toward lower wavenumbers (Wei et al., 2009).

Table 1
Bulk composition (nominal in parenthesis) of $BaFe_{1-x}Ni_xO_3$ perovskites.

Perovskites	Ba (wt %)	Fe (wt %)	Ni (wt %)
$BaFeO_3$	55.84 (56.94)	24.08 (23.16)	–
$BaFe_{0.8}Ni_{0.2}O_3$	57.25 (56.80)	19.89 (18.47)	3.17 (4.85)
$BaFe_{0.6}Ni_{0.4}O_3$	54.98 (56.67)	12.86 (13.82)	10.55 (9.68)
$BaFe_{0.4}$ $Ni_{0.6}O_3$	56.11 (56.54)	9.89 (9.19)	14.09 (14.49)
$BaFe_{0.2}Ni_{0.8}O_3$	57.14 (56.41)	3.95 (4.58)	18.98 (19.28)

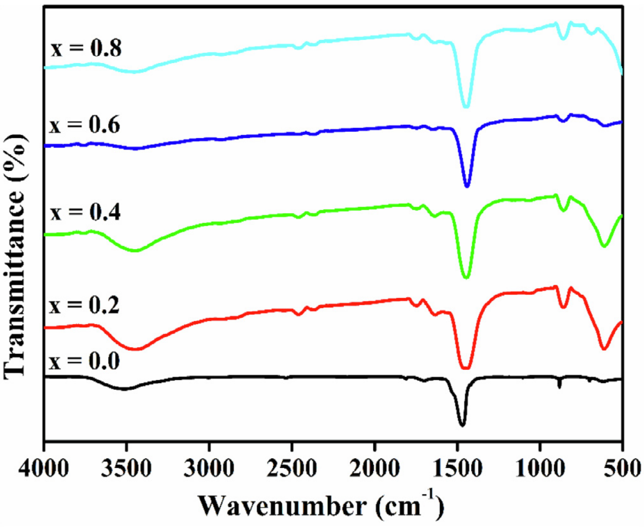

Fig. 1. FTIR spectra of series of $BaFe_{1-x}Ni_xO_3$ perovskite.

3.2. Thermal decomposition of precursors

The thermal decomposition profiles of the perovskite precursors are shown in Fig. 2. Upon increasing the Ni amount, the curves progressively shifted to a higher temperature and the decomposition occurred in three steps, which were confirmed using the DTG curves (Fig. 2(b)). The first mass loss below 200 °C is assigned to physically adsorbed water molecules and free citrate, which were identified using the IR spectra. The second major mass loss between 725 and 875 °C is attributed to the decomposition of the existing phases and the removal of organic residues. The third mass loss between 875 and 900 °C is the initiation of the crystallization process of the synthetized metal oxide phases of the perovskites. It was concluded that the total mass losses of the prepared materials were approximately 10–25%; the materials were thermally stable up to >700 °C when heated to 900 °C. Therefore, they were heated at 800 °C for 6 h to prepare the perovskite crystals.

3.3. X-ray diffraction

The XRD diffraction patterns and Rietveld refinement profiles for the pre-calcined powders are revealed in Fig. 3. The diffraction patterns consist of well-resolved peaks and match with COD ID# 41-24844. The assigned diffraction peaks corresponding to the (1 0 0), (1 1 0), (1 1 1), (2 0 0), (2 1 0), (2 1 1), and (2 2 2) reflection planes provide clear indication for the development of single-phase cubic perovskites, because there is no split of the peak around a 2θ of 44.95°, indicating that the citrate method and chosen calcination temperature (800 °C) are effective for the formation of a perovskite-type structure (Fig. 3(a)). The search-match and Rietveld-refined X-ray patterns for the perovskites are presented in Fig. 3(b)–(f). It is clear from the patterns that all the perovskites have a single-phase cubic structure; this has been indexed to the Pm-3m space group. The crystallite size, lattice parameters, unit cell volume, and R-factors such as R_p (profile factor), R_{wp} (weighted profile factor), R_{exp} (expected weighted profile factor), as well as goodness of fit (GOF) are displayed in Table 2. The variation in the lattice constants with the nickel content may be due to the substitution of Fe^{3+} ions (0.67 Å) by the relatively small Ni^{3+} (0.56) ions; however, this does not distort the structure, and causes only the contraction of the crystallite size from 15.2 to 12.7 nm as the substitution degree increases.

3.4. Optical properties

Fig. 4(a) shows the absorption spectra of the powders (transforms of the diffuse-reflection spectra). The optical response of the samples shifted from the UV to the visible-light region upon the introduction of Ni. The samples show absorption bands higher than 500 nm, implying that all the powders possess photocatalytic ability under visible-light irradiation. As shown in Fig. 4(a), the four $BaFe_{1-x}Ni_xO_3$ perovskites have a similar visible-light absorption capacity. The absorption cutoff wavelength is about 580–700 nm, indicating that they can absorb visible light effectively in the range of 420–700 nm. The strong absorption bands can be assigned to the electronic band gap transition from the valence band to the conduction band (O 2p → Fe 3d). Using the Tauc approach, the band gap values were estimated to be between 1.43 and 1.71 eV (Steiger et al., 2020; Thirumalairajan et al., 2013). The band gap energy values determined using the corresponding absorption spectra are shown in Fig. 4(b). It reduces as the Ni concentration increases, because of the variation in the particle size, and then increases for an Ni content of 0.8. Furthermore, these band gaps become more intense as per the BET specific surface area of the prepared materials increases.

3.5. Nitrogen (N_2) sorption

The textural properties determined using the BET measurements are tabulated in Table 3. $BaFeO_3$ exhibits the lowest S_{BET},

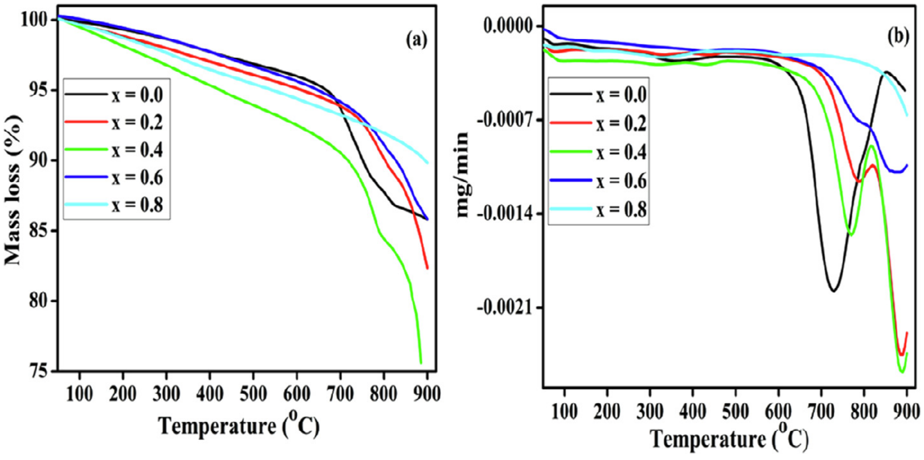

Fig. 2. TG-DTG decomposition curves of the $BaFe_{1-x}Ni_xO_3$ perovskite precursors.

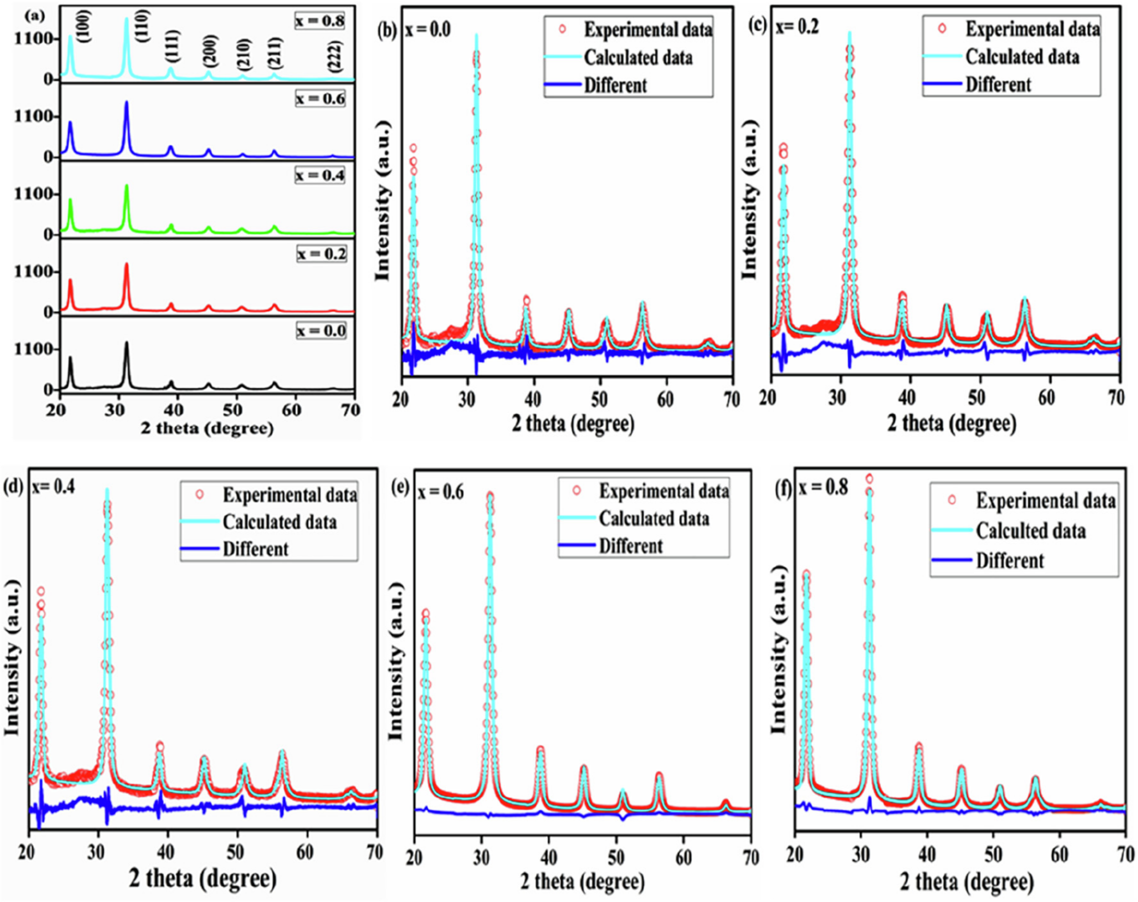

Fig. 3. XRD patterns and Rietveld refinement profile of $BaFe_{1-x}Ni_xO_3$ perovskites calcined at 800 °C.

Table 2
Structural and Rietveld refinement parameters of $BaFe_{1-x}Ni_xO_3$ perovskites.

Perovskites	Unit cell parameters (Å)			Volume(Å)^3	Crystallite size (nm)	R-factors			GOF
	a	b	c			R_p	R_{exp}	R_{wp}	
$BaFeO_3$	3.952	3.952	3.952	61.737	15.2	12.88	11.92	17.33	2.10
$BaFe_{0.8}Ni_{0.2}O_3$	3.952	3.952	3.953	61.756	14.8	9.86	10.65	12.75	1.43
$BaFe_{0.6}Ni_{0.4}O_3$	3.952	3.952	3.952	61.708	13.9	8.73	9.56	11.92	1.55
$BaFe_{0.4}Ni_{0.6}O_3$	3.947	3.947	3.947	61.498	13.4	4.39	11.70	7.22	1.32
$BaFe_{0.2}Ni_{0.8}O_3$	3.951	3.951	3.951	61.690	12.7	5.85	11.56	9.84	1.21

whereas in case of $BaFe_{1-x}Ni_xO_3$ an initial increase in the S_{BET} value was observed, which was found to decrease upon further increase of nickel content in the perovskite. The low surface area exhibited by these materials may seem abnormal based on the literature (Escalona et al., 2010; Leanza et al., 2000). The reason for the higher S_{BET} for $BaFe_{0.8}Ni_{0.2}O_3$ as compared with those of the other perovskites can be understood using the PSD and *V*p. The higher *V*p of $BaFe_{0.8}Ni_{0.2}O_3$ is consistent with the higher $S_{BET.}$ The N_2 adsorption–desorption isotherms and their Pore size distribution profiles presents in Fig. 5(a) and (b). These isotherms are type IV at high relative pressures ($0.6 < P/P_o < 0.8$), which are characteristics of mesoporosity (Yao et al., 2018). The hysteresis loop for the relative pressure range used indicates mesoporous diameter, which likely resulted from aggregated pores. Moreover, it was noted that the Ni amounts could affect the hysteresis loops. $BaFeO_3$ and $BaFe_{0.2}Ni_{0.8}O_3$ exhibit similar typical type IV isotherms and H2-type hysteresis loops for P/P_o between 0.6 and 0.9, indicating the formation of ordered mesoporous structures due to the accumulation of nanoparticles (Huang et al., 2015). The other isotherms clearly show H3-type hysteresis loops when P/P_o is in the range of 0.7–1.0. This indicates that slit-like pores are generated in these materials owing to the agglomerated particles. This is in agreement with the analysis of the TEM images.

In addition, the PSD was calculated from the isotherms using the BJH method (Fig. 5(b)). Obviously, markedly developed porous structures produced in each fabricated perovskite, and the pore distribution was strongly related to the amounts of Ni. A sharp pore volume distribution in a narrow and small pore diameter range was observed for low Ni contents, whereas the high Ni contents samples showed broad peaks for larger pore diameters.

3.6. Morphological properties

The general morphology and microstructures of the different catalysts were analyzed using TEM, and are demonstrated in Fig. 6(a)–(e). It was found that each sample is made of aggregated particles of irregular morphologies. The extent of agglomeration increases with Ni content. The figure clearly shows that there are

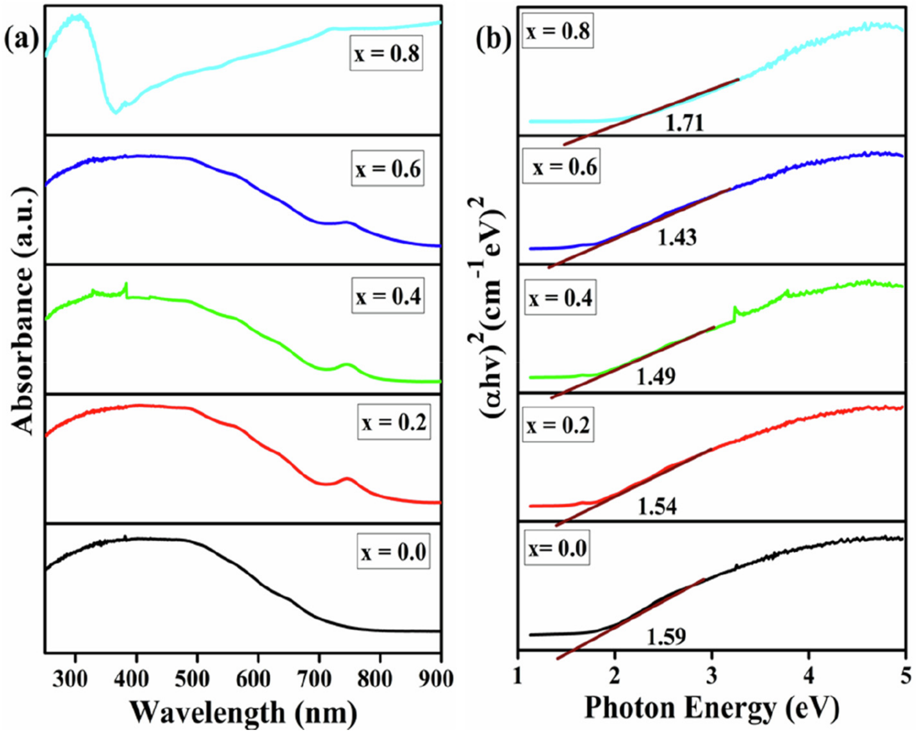

Fig. 4. UV–vis absorption spectra (a) and band gap energy (b) of $BaFe_{1-x}Ni_xO_3$ perovskites.

Table 3
Textural properties and porosity parameters of $BaFe_{1-x}Ni_xO_3$ perovskites.

Perovskites	S_{BET} (m^2/g)	Pore volume (cm^3/g)	Pore size (nm)
$BaFeO_3$	14.072	0.079	27.069
$BaFe_{0.8}Ni_{0.2}O_3$	27.608	0.160	26.358
$BaFe_{0.6}Ni_{0.4}O_3$	23.847	0.119	23.013
$BaFe_{0.4} Ni_{0.6}O_3$	21.765	0.133	26.073
$BaFe_{0.2}Ni_{0.8}O_3$	16.116	0.078	23.515

no remarkable differences in the shape of the substituted materials; most of the nanoparticles have a diameter in the range of 10–30 nm and a smooth surface. The particle sizes of the calcined powders are around 19–25, 10–15, 12–25, 8–12, and 15–30 nm for x = 0.0, 0.2, 0.4, 0.6, and 0.8, respectively. The size of the nanoparticles increases with the Ni amount. The particle size are larger than the crystallite sizes calculated from the XRD patterns (12–16 nm), implying that each particle is possibly composed of various crystallites.

The scanning electron micrograph of the highly active catalyst $BaFe_{0.4}Ni_{0.6}O_3$ is shown in Fig. 6(f). The particles (~10–25 nm) are not regular, and they join together to form a honeycomb structure. There are a large number of pores, which is favorable for catalytic BzOH oxidation.

3.7. Temperature-programmed reduction (H_2-TPR) and oxidation (O_2-TPO)

To investigate the degree of interaction between the active metals (Fe and Ni) in the prepared catalysts, H_2-TPR experiments were carried out. The H_2-TPR profiles of each catalyst are revealed in Fig. 7(a). Two reduction peaks were detected, and could be ascribed to the stepwise reduction of the samples. The $BaFeO_3$

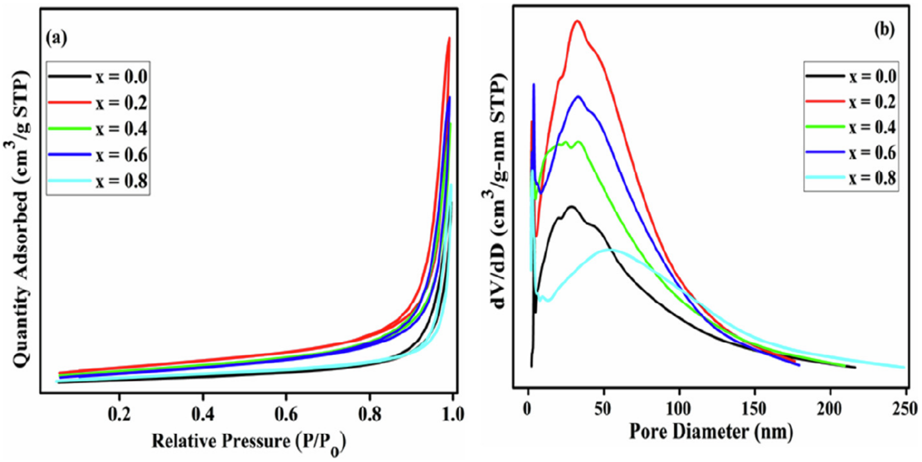

Fig. 5. N_2 adsorption-desorption isotherms (a) and pore-size distribution curves (b) of $BaFe_{1-x}Ni_xO_3$.

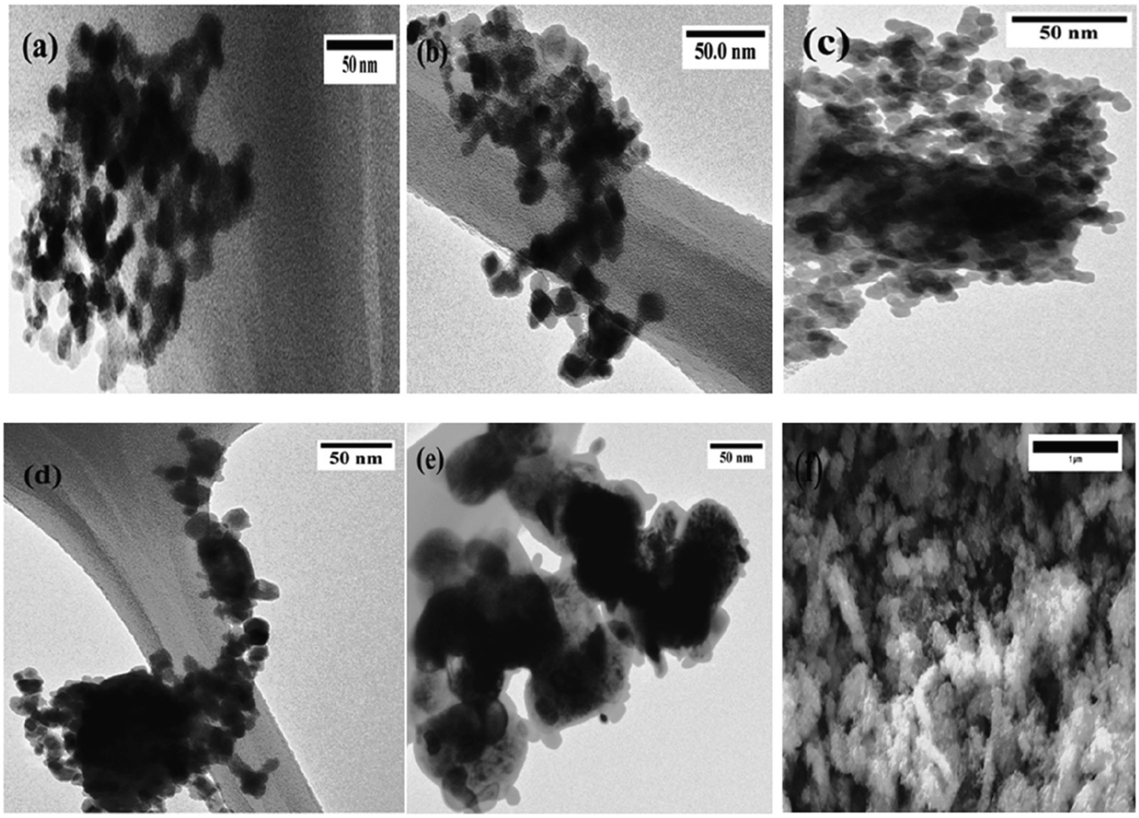

Fig. 6. TEM and SEM images of the synthesized perovskites: (a) $BaFeO_3$ (b) $BaFe_{0.2}Ni_{0.8}O_3$ (c) $BaFe_{0.4}Ni_{0.6}O_3$ (d) $BaFe_{0.6}Ni_{0.4}O_3$ and (e & f) $BaFe_{0.8}Ni_{0.2}O_3$.

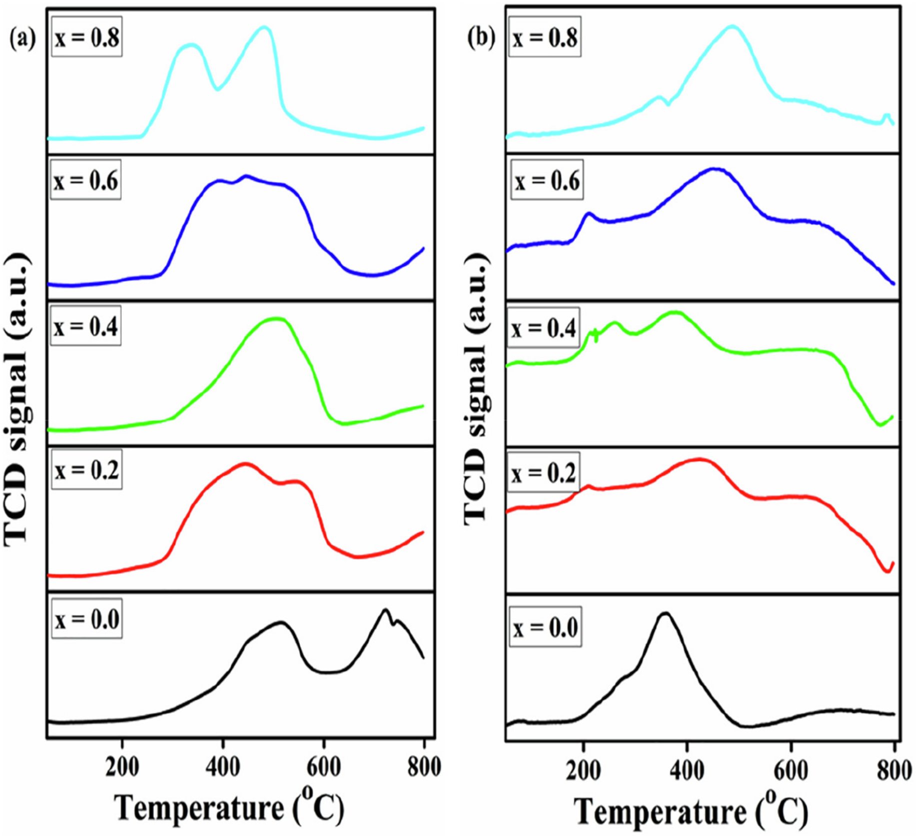

Fig. 7. TPR (a) and TPO (b) profiles of $BaFe_{1-x}Ni_xO_3$ perovskites calcined at 1073 K.

sample underwent reduction in two steps, with the first maxima centered at 510 °C and the second positioned at 725 °C with a small shoulder at 750 °C. The first peak has been allocated to the reduction of Fe^{3+} to Fe^{2+} on the surface, whereas the other peak is attributed to the reduction of Fe^{2+} to Fe^0 in the bulk. The Fe-substituted samples present similar reduction patterns. For substituted $BaFe_{1-x}Ni_xO_3$, except $BaFe_{0.2}Ni_{0.8}O_3$, the first peak became wider and shifted toward a lower temperature and the next peak shifted to a higher temperature because of the weak and strong metal–metal interactions during the reduction process. $BaFe_{0.2}Ni_{0.8}O_3$ exhibits two highly intense reduction peaks at 335 and 485 °C, indicating that there are two kinds of oxide species existing on the exterior of this catalyst and that it has a higher reducibility than that of the other prepared catalysts. According to Ruckenstein, the low-temperature peaks are not attributable to $LaBO_3$ (B, Ni or Fe) but for the reduction of its amorphous oxides (Ruckenstein and Hu, 1996), and the high-temperature peaks are consequently of the reduction of the perovskite phases. The reduced catalyst can be regenerated with O_2; however, the oxidation is not complete under the chosen conditions (Fig. 7(b)).

3.8. Temperature programmed desorption (CO_2-TPD)

The basic strength of the perovskites is shown in Fig. 8. It was evaluated using CO_2-TPD in terms of the chemisorption of the acidic gas (CO_2) on the available basic sites of the samples and desorption in a programmed temperature range (100–900 °C). According to the observed adsorption–desorption phenomenon, the adsorbate that was adsorbed on weaker basic sites desorbed at lower temperatures, while those on stronger basic sites desorbed at higher temperatures. Depending on the desorption temperature, the basic strength was categorized into weak (<200 °C), moderate (200–400 °C), and strong (>400 °C) (Istadi and Saidina Amin, 2006). The difference in the TPD patterns is due to the difference in the CO_2 adsorption capacity of these catalysts. However, these the catalysts show two distinct CO_2 desorption peaks, except the $BaFe_{0.2}Ni_{0.8}O_3$ catalyst, which shows no considerable CO_2 desorption peak. The first peak appeared between ~ 500 and 700 °C and the second between 700 and 900 °C. In this case, a signal was also found above 800 °C, indicating that the liberation of CO_2 was still occurring. Moreover, the desorption peak temperatures shifted with a variation in the x values. In particular, the CO_2-TPD spectrum for the Ba $Fe_{0.6}Ni_{0.4}O_3$ sample shows two small shoulders at 655 and 725 °C.

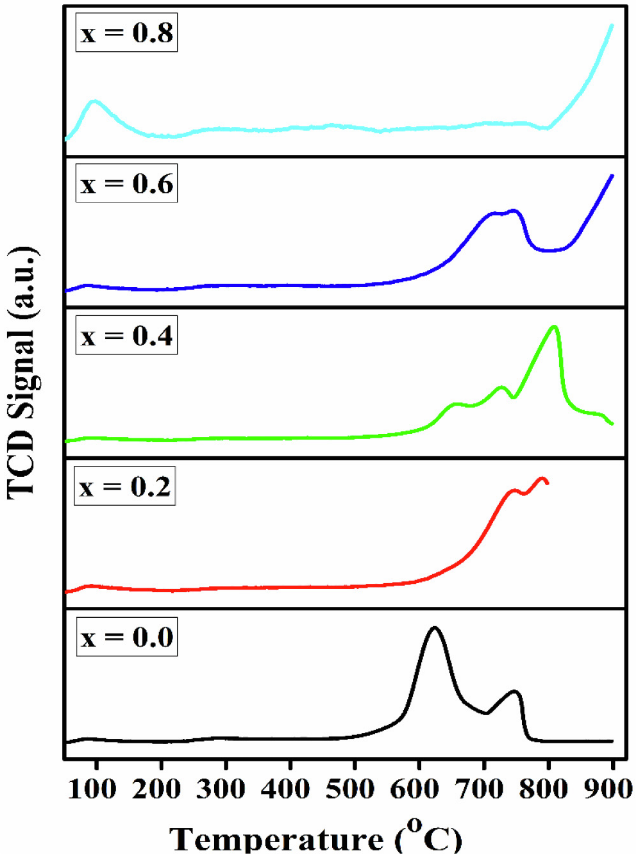

Fig. 8. CO_2-TPD profiles of $BaFe_{1-x}Ni_xO_3$ perovskites calcined at 1073 K.

3.9. Catalytic performance

3.9.1. Catalytic activity

Fig. 9 shows the catalytic behavior of the perovskites. It was evaluated in terms of the BzOH conversion with the time on stream at 100 °C; the obtained data are compiled in Table 4. All the catalysts show high selectivity toward BzH, with a negligible amount of benzoic acid as the byproduct, within the allowed reaction duration. $BaFeO_3$ shows the poorest conversion; however, the incorporation of nickel into $BaFeO_3$ significantly improves the catalytic behavior, and a 99.9% BzH selectivity is maintained. The BzOH conversions increased when the nickel amount was increased from 0.2 to 0.6 in the catalysts, due to the synergic interaction between Ni and Fe cations with the collaboration of lattice oxygen (Behera and Parida, 2012), as well as the chemisorption of oxygen species. However, a further increase in the Ni amount caused a minor decrease in the catalytic behavior because excess amounts of nickel covered the active sites of the catalyst ($BaFe_{0.2}Ni_{0.8}O_3$). There was no direct relationship between the porosity and catalytic performance results of the prepared catalysts, even though the difference in the S_{BET} values of the catalysts was small. Hence, the surface area was not a determining factor for the activities of the prepared perovskites. Among the studied catalysts, $BaFe_{0.4}Ni_{0.6}O_3$ was the most active catalytic agent, with a specific activity of 0.34 mmol g^{-1} h^{-1} and a TOF of 3.28 h^{-1}, and it was chosen for subsequent studies.

3.9.2. Recyclability testing of $BaFe_{0.4}Ni_{0.6}O_3$ catalyst

Recyclability is an essential factor for industrial uses. To evaluate the recyclability of the selected catalyst, the BzOH oxidation

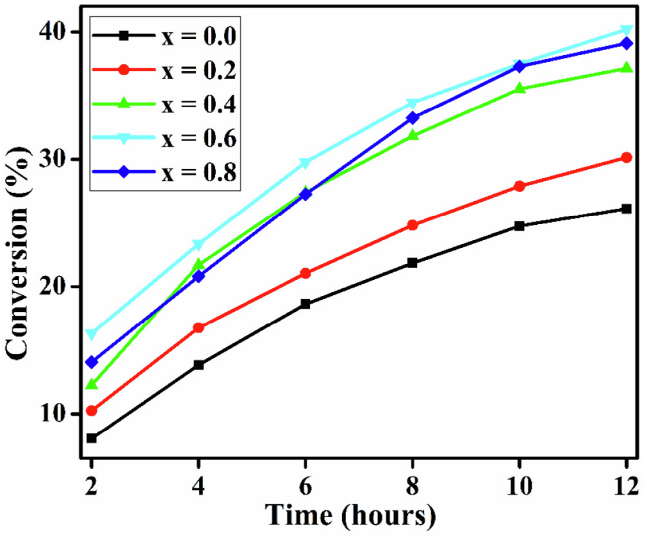

Fig. 9. Conversion of $BaFe_{1-x}Ni_xO_3$ catalysts as a function of time.

Table 4
The catalytic performance of $BaFe_{1-x}Ni_xO_3$ catalysts.[a]

Catalysts	Conversion (%)	Selectivity (%)	Specific activity (mmol g^{-1} h^{-1})	TON	TOF (h^{-1})
$BaFeO_3$	26.33	99<	0.22	–	–
$BaFe_{0.8}Ni_{0.2}O_3$	30.15	99<	0.25	88.42	7.36
$BaFe_{0.6}Ni_{0.4}O_3$	37.16	99<	0.31	54.65	4.60
$BaFe_{0.4}Ni_{0.6}O_3$	40.20	99<	0.34	39.41	3.28
$BaFe_{0.2}Ni_{0.8}O_3$	39.12	99<	0.33	28.98	2.42

[a] Reaction conditions: catalyst, 200 mg; benzyl alcohol, 2 mmol; O_2, 20 mL min^{-1}; toluene, 10 mL; temperature, 100 °C; time, 12 h.

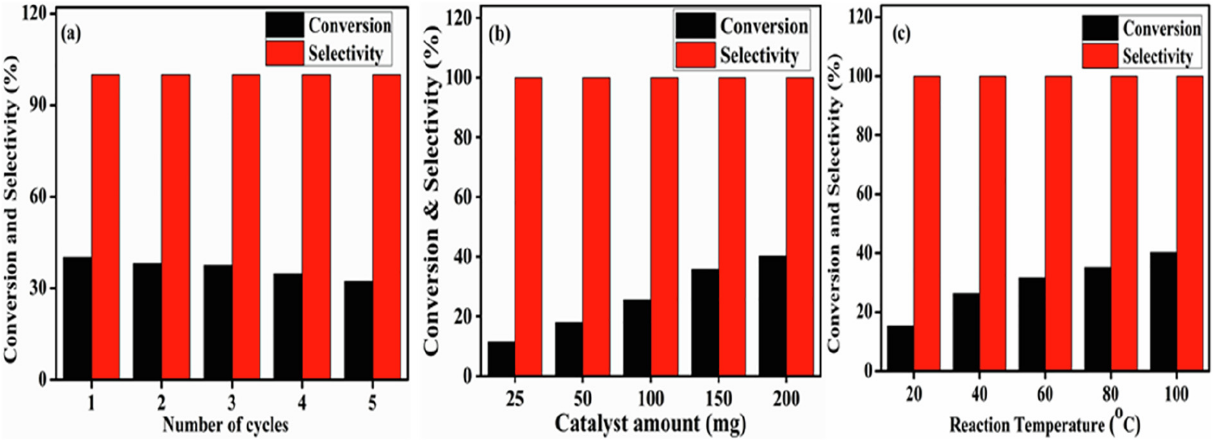

Fig. 10. Benzyl alcohol oxidation as a function of (a) cycle number (b) amount (c) temperature on $BaFe_{0.4}Ni_{0.6}O_3$ catalyst.

Table 5
The catalytic performance with different reaction parameters of the $BaFe_{0.4}Ni_{0.6}O_3$ catalyst.[a]

Parameter	Variables	Conversion (%)	Selectivity (%)	Specific activity (mmol g^{-1} h^{-1})	TON	TOF (h^{-1})
Recycling	1	40.2	<99	0.34	39.41	3.28
	2	38.04	<99	0.32	37.21	3.1
	3	37.5	<99	0.31	36.68	3.06
	4	34.85	<99	0.29	34.09	2.84
	5	32.31	<99	0.27	31.6	2.63
Catalyst amount (mg)	25	11.38	>99	0.76	91.04	7.59
	50	17.97	>99	0.60	70.47	5.87
	100	25.56	>99	0.43	50.18	4.18
	150	35.78	>99	0.40	46.77	3.90
	200	40.2	>99	0.34	39.41	3.28
Temperature (°C)	20	15.39	>99	0.13	15.05	1.25
	40	26.33	>99	0.22	25.76	2.15
	60	31.56	>99	0.26	30.87	2.75
	80	35.12	>99	0.29	34.35	2.86
	100	40.20	>99	0.34	39.41	3.28

[a] Reaction conditions: benzyl alcohol, 2 mmol; O_2, 20 mL min^{-1}, toluene, 10 mL; time, 12 h.

was run five times under the identical reaction conditions; the results are illustrated in Fig. 10(a) and summarized in Table 5. The $BaFe_{0.4}Ni_{0.6}O_3$ catalyst did not show a noticeable change in the activity after 12 h and the BzH selectivity remained constant throughout the runs, which verified that no leaching of the metals occurred during the reactions. During the recyclability testing, the slight decrease in the BzOH conversion from 40.20 to 32.31% may have been due to the mass loss during the centrifugation process. Therefore, this catalyst exhibits excellent recyclability.

3.9.3. Effects of reaction conditions on catalytic behavior

The influences of the reaction conditions, catalyst amount, and reaction temperature on the effectiveness of $BaFe_{0.4}Ni_{0.6}O_3$ catalyst are summarized in Table 5 and illustrated in Fig. 10(b) and (c). For the determination of the influence of the catalyst quantity on the catalytic activity of $BaFe_{0.4}Ni_{0.6}O_3$, the amount was varied (25–200 mg) while the other reaction conditions were kept constant. There was a direct correlation between the conversion and the catalyst amount. The low conversion of BzOH into BzH at low catalyst amounts (25 and 50 mg) may have been due to the low availability of catalyst sites. An inverse correlation between the specific activity and the catalyst amount was deduced while the selectivity persevered during the studies.

The influence of the temperature on the selectivity and conversion was determined using five different reaction temperatures; the results are summarized in Table 5 and illustrated in Fig. 10 (c). It was observed that on increasing the temperature (20–100 °C), the product selectivity of the $BaFe_{0.4}Ni_{0.6}O_3$ catalytic agent remained unchanged (>99%), whereas the BzOH conversion increased from 15.39 to 40.2%. This was because higher temperatures contributed to higher oxidation rates, which improved the catalytic activity, whereas at low temperatures, the conversion was kinetically controlled due to the intrinsic thermal effect (Chaudhari and Sawant, 2005). In addition, the specific activity,

Table 6
A comparison between the as-prepared catalyst and other reported catalysts for the catalytic oxidation of BzOH to BzH.

Catalyst	Conv. (%)	Sel. (%)	Temp. (°C)	t. (h)	TOF (h^{-1})	Sp. activity (mmol g^{-1} h^{-1})	Ref.
$BaFe_{0.4}Ni_{0.6}O_3$	40	<99	100	12	3.28	0.34	Herein
CuZnO	<99	<99	RT	3	48.31	33.33	(Forouzani et al., 2015)
Au NPs/CuO–ZnO	94	<99	RT	1	–	18.80	(Albadi et al., 2014)
Cu-Mn_2 oxide	100	<99	102	1.3	2.83	15.00	(Ali et al., 2015)
Au(0)–zeolite	<95	<99	80	5	11.0	0.63	(Zahmakıran and Özkar, 2010)
MnO_2/GRO	98	100	110	4	1.17	1.23	(Hu et al., 2016)
AuPd NPs - GRO/TiO_2	89	69	120	2	41.0	–	(Wang et al., 2015)
Ag–MnO_2–Au	100	<99	100	1.5	13.55	4.44	(Alabbad et al., 2014)
Mn/Al_2O_3	93	<99	100	4	0.50	0.93	(Tang et al., 2009)
Au NPs/HT	57	94	40	24	9.61	0.96	(Yu et al., 2014)
Ag NPs/GOSH	61	58	80	24	5.72	5.08	(Zahed and Hosseini-Monfared, 2015)
Au/CuO–MCM	73	94	80	20	7.40	0.86	(Wang et al., 2013)
Cell-Pd NPs	100	82	80	15	22.22	0.22	(Jamwal et al., 2011)

TOF, and TON increased when the reaction temperature was increased. Consequently, in this investigation, 100 °C was designated as the finest temperature to attain the highest catalytic activity. It is important to mention here that when the catalytic performance evaluation was carried out in the absence of the $BaFe_{0.4}Ni_{0.6}O_3$ catalyst under similar parameters, there was no formation of target product (BzH). Similarly, to rule out the BzH formation via the oxidation of the solvent (toluene), a reaction was carried out in the absence of the substrate (BzOH), and again, no conversion product was formed. The activation energy of the catalyst was calculated by plotting the logarithm of the BzOH conversion rate against the reciprocal of the reaction temperature (not shown), and was found to be 10.25 J mol^{-1} K^{-1}, inferring that the BzOH oxidation over $BaFe_{0.4}Ni_{0.6}O_3$ would require severe conditions (T, P, and catalytic amount) for a better yield of the target product.

Furthermore, to illustrate the outstanding catalytic effectiveness of the present catalytic methodology, the catalytic activity of the as-prepared catalyst has been compared with other reported catalysts that found in the previously literature is collected in Table 6.

4. Conclusions

In this study, cubic-phase $BaFe_{1-x}Ni_xO_3$ catalysts were successfully synthesized via a simple chemical route, which can be extended for the preparation of other perovskites. X-ray diffraction and subsequent Rietveld refinement revealed successful substitution of Ni ions at Fe sites. The synthesized materials exhibited good structural, optical, and surface properties. To explore the catalytic oxidations of the fabricated perovskites, a comparative investigation was carried out. The synergistic interactions between the hybrid active sites (through oxygen) and the Fe/Ni molar ratio played essential roles in promoting the catalytic efficiency for alcohol oxidation. During this study, $BaFe_{0.4}Ni_{0.6}O_3$ displayed a better catalytic capacity than other $BaFe_{1-x}Ni_xO_3$ perovskites.

Declaration of Competing Interest

The authors declare that they have no known competing financial interests or personal relationships that could have appeared to influence the work reported in this paper.

Acknowledgment

The authors are grateful to the Researchers Supporting Project number (RSP-2019/113), King Saud University, Riyadh, Saudi Arabia for the support.

Appendix A. Supplementary data

Supplementary data to this article can be found online at https://doi.org/10.1016/j.jksus.2020.02.015.

References

Abdolrahmani, M., Parvari, M., Habibpoor, M., 2010. Effect of copper substitution and preparation methods on the $LaMnO_{3\pm\delta}$ structure and catalysis of methane combustion and CO oxidation. Chin. J. Catal. 31, 394–403.

Alabbad, S., Adil, S., Assal, M., Khan, M., Alwarthan, A., Siddiqui, M.R.H., 2014. Gold & silver nanoparticles supported on manganese oxide: synthesis, characterization and catalytic studies for selective oxidation of benzyl alcohol. Arab. J. Chem. 7, 1192–1198.

Albadi, J., Alihoseinzadeh, A., Razeghi, A., 2014. Novel metal oxide nanocomposite of Au/CuO–ZnO for recyclable catalytic aerobic oxidation of alcohols in water. Catal. Commun. 49, 1–5.

Ali, R., Nour, K., Al-warthan, A., Siddiqui, M.R.H., 2015. Selective oxidation of benzylic alcohols using copper-manganese mixed oxide nanoparticles as catalyst. Arab. J. Chem. 8, 512–517.

Alifanti, M., Auer, R., Kirchnerova, J., Thyrion, F., Grange, P., Delmon, B., 2003. Activity in methane combustion and sensitivity to sulfur poisoning of $La_{1-x}Ce_xMn_{1-y}Co_yO_3$ perovskite oxides. Appl. Catal. B Environ. 41, 71–81.

Arakawa, T., Kurachi, H., Shiokawa, J., 1985. Physicochemical properties of rare earth perovskite oxides used as gas sensor material. J. Mater. Sci. 20, 1207–1210.

Assal, M.E., Shaik, M.R., Kuniyil, M., Khan, M., Al-Warthan, A., Alharthi, A.I., Varala, R., Siddiqui, M.R.H., Adil, S.F., 2019. Ag_2O nanoparticles/$MnCO_3$, –MnO_2 or –Mn_2O_3/highly reduced graphene oxide composites as an efficient and recyclable oxidation catalyst. Arab. J. Chem. 12, 54–68.

Attaoua, M., Beriala, S., Omari, M., 2012. Defect chemistry and physical properties of $Ln_{0.5}Sr_{0.5}FeO_3$ (Ln: La, Pr). J. Saudi Chem. Soc. 16, 91–95.

Behera, G.C., Parida, K., 2012. Liquid phase catalytic oxidation of benzyl alcohol to benzaldehyde over vanadium phosphate catalyst. Appl. Catal. A 413, 245–253.

Berger, D., Matei, C., Papa, F., Voicu, G., Fruth, V., 2007. Pure and doped lanthanum cobaltites obtained by combustion method. Prog. Solid State Chem. 35, 183–191.

Chaudhari, M.P., Sawant, S.B., 2005. Kinetics of heterogeneous oxidation of benzyl alcohol with hydrogen peroxide. Chem. Eng. J. 106, 111–118.

Choudhary, V.R., Dhar, A., Jana, P., Jha, R., Uphade, B.S., 2005. A green process for chlorine-free benzaldehyde from the solvent-free oxidation of benzyl alcohol with molecular oxygen over a supported nano-size gold catalyst. Green Chem. 7, 768–770.

Enache, D.I., Edwards, J.K., Landon, P., Solsona-Espriu, B., Carley, A.F., Herzing, A.A., Watanabe, M., Kiely, C.J., Knight, D.W., Hutchings, G.J., 2006. Solvent-free oxidation of primary alcohols to aldehydes using Au-Pd/TiO_2 catalysts. Science 311, 362–365.

Escalona, N., Fuentealba, S., Pecchi, G., 2010. Fischer-Tropsch synthesis over $LaFe_{1-x}Co_xO_3$ perovskites from a simulated biosyngas feed. Appl. Catal.A 381, 253–260.

Ferguson, G., Ajjou, A.N., 2003. Solvent-free oxidation of alcohols by t-butyl hydroperoxide catalyzed by water-soluble copper complex. Tetrahedron Lett. 44, 9139–9142.

Forni, L., Oliva, C., Vatti, F., Kandala, M., Ezerets, A., Vishniakov, A., 1996. LaCeCo perovskites as catalysts for exhaust gas depollution. Appl. Catal. B Environ. 7, 269–284.

Forouzani, M., Mardani, H.R., Ziari, M., Malekzadeh, A., Biparva, P., 2015. Comparative study of oxidation of benzyl alcohol: influence of Cu-doped metal cation on nano ZnO catalytic activity. Chem. Eng. J. 275, 220–226.

Gajbhiye, N., Bhattacharya, U., Darshane, V., 1995. Thermal decomposition of zinc-iron citrate precursor. Thermochim. Acta 264, 219–230.

Gallagher, P., Johnson Jr, D., Vogel, E., 1977. Preparation, structure, and selected catalytic properties of the system $LaMn_{1-x}Cu_xO_{3-y}$. J. Am. Ceram. Soc. 60, 28–31.

Ghasdi, M., Alamdari, H., Royer, S., Adnot, A., 2011. Electrical and CO gas sensing properties of nanostructured $La_{1-x}Ce_xCoO_3$ perovskite prepared by activated reactive synthesis. Sens. Actuators B Chem. 156, 147–155.

Haruna, A., Abdulkadir, I., Idris, S., 2019. Synthesis, characterization and photocatalytic properties of $Bi_{0.85-X}M_XBa_{0.15}FeO_3$ (M = Na and K, X = 0, 0.1) perovskite-like nanoparticles using the sol-gel method. J. King Saud Univ. Sci.

Hashemian, S., Foroghimoqhadam, A., 2014. Effect of copper doping on $CoTiO_3$ ilmenite type nanoparticles for removal of congo red from aqueous solution. Chem. Eng. J. 235, 299–306.

Hu, Z., Zhao, Y., Liu, J., Wang, J., Zhang, B., Xiang, X., 2016. Ultrafine MnO_2 nanoparticles decorated on graphene oxide as a highly efficient and recyclable catalyst for aerobic oxidation of benzyl alcohol. J. Colloid Interface Sci. 483, 26–33.

Huang, X., Sun, N., Xue, G., Wang, C., Zhan, H., Zhao, N., Xiao, F., Wei, W., Sun, Y., 2015. Effect of pore geometries on the catalytic properties of $NiO–Al_2O_3$ catalysts in CO_2 reforming of methane. RSC Adv. 5, 21090–21098.

Islam, S., Bakhtiar, H., Bidin, N., Salim, A.A., Riaz, S., Abbas, K.N., Suan, L.P., Naseem, S., 2018. Influence of ZnO doping on structural, optical and pH-stimulus characteristics of silica-titania nanocomposite matrix. J. Saudi Chem. Soc. 22, 826–837.

Istadi, I., Saidina Amin, N., 2006. Synergistic effect of catalyst basicity and reducibility on performance of ternary CeO_2-based catalyst for CO_2 OCM to C_2 hydrocarbons. J. Mol. Catal. A Chem. 259, 61–66.

Jamwal, N., Sodhi, R.K., Gupta, P., Paul, S., 2011. Nano Pd (0) supported on cellulose: a highly efficient and recyclable heterogeneous catalyst for the Suzuki coupling and aerobic oxidation of benzyl alcohols under liquid phase catalysis. Int. J. Biol. Macromol. 49, 930–935.

Karimi, L., Zohoori, S., Yazdanshenas, M.E., 2014. Photocatalytic degradation of azo dyes in aqueous solutions under UV irradiation using nano-strontium titanate as the nanophotocatalyst. J. Saudi Chem. Soc. 18, 581–588.

Leanza, R., Rossetti, I., Fabbrini, L., Oliva, C., Forni, L., 2000. Perovskite catalysts for the catalytic flameless combustion of methane: Preparation by flame-hydrolysis and characterisation by TPD–TPR-MS and EPR. Appl. Catal. B Environ. 28, 55–64.

Liu, G., Geng, Y., Pan, D., Zhang, Y., Niu, T., Liu, Y., 2014. Bi-metal Cu–Co from $LaCo_{1-x}Cu_xO_3$ perovskite supported on zirconia for the synthesis of higher alcohols. Fuel Process. Technol. 128, 289–296.

Luo, J., Yu, H., Wang, H., Wang, H., Peng, F., 2014. Aerobic oxidation of benzyl alcohol to benzaldehyde catalyzed by carbon nanotubes without any promoter. Chem. Eng. J. 240, 434–442.

Ma, A.-J., Wang, S.-Z., Liu, C., Xian, H., Ding, Q., Guo, L., Meng, M., Tan, Y.-S., Tsubaki, N., Zhang, J., 2014. Effects of Fe dopants and residual carbonates on the catalytic activities of the perovskite-type $La_{0.7}Sr_{0.3}Co_{1-x}Fe_xO_3$ NO_x storage catalyst. Appl. Catal. B Environ. 146, 24–34.

Madduluri, V.R., Nagaiah, P., Prathap, C., Gidyonu, P., Raju, B.D., Rao, K.S.R., 2019. La_2O_3 promotional effect to Co_3O_4/γ-Al_2O_3 catalyst in the oxidative dehydrogenation of ethylbenzene with CO_2 as soft oxidant. J. Saudi Chem. Soc. 23, 678–690.

Mallat, T., Baiker, A., 2004. Oxidation of alcohols with molecular oxygen on solid catalysts. Chem. Rev. 104, 3037–3058.

Merino, N.A., Barbero, B.P., Grange, P., Cadús, L.E., 2005. $La_{1-x}Ca_xCoO_3$ perovskite-type oxides: preparation, characterisation, stability, and catalytic potentiality for the total oxidation of propane. J. Catal. 231, 232–244.

Mitran, G., Mieritz, D.G., Seo, D.-K., 2019. Steam reforming of toluene as model of tar compound over Mo catalysts derived from hydrotalcites. J. Saudi Chem, Soc.

Opre, Z., Ferri, D., Krumeich, F., Mallat, T., Baiker, A., 2006. Aerobic oxidation of alcohols by organically modified ruthenium hydroxyapatite. J. Catal. 241, 287–295.

Pan, L., Zhu, X.-D., Xie, X.-M., Liu, Y.-T., 2015. Delicate ternary heterostructures achieved by hierarchical co-assembly of Ag and Fe_3O_4 nanoparticles on MoS_2 nanosheets: morphological and compositional synergy in reversible lithium storage. J. Mater. Chem. A 3, 2726–2733.

Pena, M., Fierro, J., 2001. Chemical structures and performance of perovskite oxides. Chem. Rev. 101, 1981–2018.

Peyrovi, M., Mahdavi, V., Salehi, M., Mahmoodian, R., 2005. Oxidation of alcohols with tert-butylhydroperoxide catalyzed by Co (II) complexes immobilized between silicate layers of bentonite. Catal. Commun. 6, 476–479.

Ponce, S., Pena, M., Fierro, J., 2000. Surface properties and catalytic performance in methane combustion of Sr-substituted lanthanum manganites. Appl. Catal. B Environ. 24, 193–205.

Royer, S., Berube, F., Kaliaguine, S., 2005. Effect of the synthesis conditions on the redox and catalytic properties in oxidation reactions of $LaCo_{1-x}Fe_xO_3$. Appl. CatalA 282, 273–284.

Royer, S., Duprez, D., Can, F., Courtois, X., Batiot-Dupeyrat, C., Laassiri, S., Alamdari, H., 2014. Perovskites as substitutes of noble metals for heterogeneous catalysis: dream or reality. Chem. Rev. 114, 10292–10368.

Ruckenstein, E., Hu, Y., 1996. Interactions between Ni and La_2O_3 in Ni/La_2O_3 catalysts prepared using different Ni precursors. J. Catal. 161, 55–61.

Sawayama, Y.-S., Shibahara, H., Ichihashi, Y., Nishiyama, S., Tsuruya, S., 2006. Promoting effect and role of alkaline earth metal added to supported Ag catalysts in the gas-phase catalytic oxidation of benzyl alcohol. Ind. Eng. Chem. Res. 45, 8837–8845.

Sheldon, R.A., Arends, I., Dijksman, A., 2000. New developments in catalytic alcohol oxidations for fine chemicals synthesis. Catal. Today 57, 157–166.

Steiger, P., Kröcher, O., Ferri, D., 2020. Increased nickel exsolution from $LaFe_{0.8}Ni_{0.2}O_3$ perovskite-derived CO_2 methanation catalysts through strontium doping. Appl. Catal. A 590, 117328.

Su, F.Z., Liu, Y.M., Wang, L.C., Cao, Y., He, H.Y., Fan, K.N., 2008. Ga–Al mixed-oxide-supported gold nanoparticles with enhanced activity for aerobic alcohol oxidation. Angew. Chem. Int. Ed. 120, 340–343.

Szabo, V., Bassir, M., Gallot, J., Van Neste, A., Kaliaguine, S., 2003. Perovskite-type oxides synthesised by reactive grinding: Part III. Kinetics of n-hexane oxidation over $LaCo_{(1-x)}FexO_3$. Appl. Catal. B Environ. 42, 265–277.

Tang, Q., Gong, X., Wu, C., Chen, Y., Borgna, A., Yang, Y., 2009. Insights into the nature of alumina-supported MnOOH and its catalytic performance in the aerobic oxidation of benzyl alcohol. Catal. Commun. 10, 1122–1126.

Thirumalairajan, S., Girija, K., Hebalkar, N.Y., Mangalaraj, D., Viswanathan, C., Ponpandian, N., 2013. Shape evolution of perovskite $LaFeO_3$ nanostructures: a systematic investigation of growth mechanism, properties and morphology dependent photocatalytic activities. RSC Adv. 3, 7549–7561.

Thirumalairajan, S., Girija, K., Mastelaro, V.R., Ponpandian, N., 2014. Photocatalytic degradation of organic dyes under visible light irradiation by floral-like $LaFeO_3$ nanostructures comprised of nanosheet petals. New J. Chem. 38, 5480–5490.

Wang, H., Fan, W., He, Y., Wang, J., Kondo, J.N., Tatsumi, T., 2013. Selective oxidation of alcohols to aldehydes/ketones over copper oxide-supported gold catalysts. J. Catal. 299, 10–19.

Wang, J., Kondrat, S.A., Wang, Y., Brett, G.L., Giles, C., Bartley, J.K., Lu, L., Liu, Q., Kiely, C.J., Hutchings, G.J., 2015. Au–Pd nanoparticles dispersed on composite titania/graphene oxide-supports as a highly active oxidation catalyst. ACS Catal. 5, 3575–3587.

Wei, Z.-X., Xu, Y.-Q., Liu, H.-Y., Hu, C.-W., 2009. Preparation and catalytic activities of $LaFeO_3$ and Fe_2O_3 for HMX thermal decomposition. J. Hazard. Mater. 165, 1056–1061.

Xiao, P., Hong, J., Wang, T., Xu, X., Yuan, Y., Li, J., Zhu, J., 2013. Oxidative degradation of organic dyes over supported perovskite oxide $LaFeO_3$/SBA-15 under ambient conditions. Catal. Lett. 143, 887–894.

Yamamoto, R., Sawayama, Y.-S., Shibahara, H., Ichihashi, Y., Nishiyama, S., Tsuruya, S., 2005. Promoted partial oxidation activity of supported Ag catalysts in the gas-phase catalytic oxidation of benzyl alcohol. J. Catal. 234, 308–317.

Yang, X., Fu, J., Jin, C., Chen, J., Liang, C., Wu, M., Zhou, W., 2010. Formation mechanism of $CaTiO_3$ hollow crystals with different microstructures. J. Am. Chem. Soc. 132, 14279–14287.

Yao, G., Wu, L., Lv, T., Li, J., Huang, Y., Dong, K., Li, X., 2018. The effect of CuO modification for a TiO_2 nanotube confined CeO_2 catalyst on the catalytic combustion of butane. Open Chem. 16, 1–8.

Yu, J., Li, J., Wei, H., Zheng, J., Su, H., Wang, X., 2014. Hydrotalcite-supported gold catalysts for a selective aerobic oxidation of benzyl alcohol driven by visible light. J. Mol. Catal. A Chem. 395, 128–136.

Zahed, B., Hosseini-Monfared, H., 2015. A comparative study of silver-graphene oxide nanocomposites as a recyclable catalyst for the aerobic oxidation of benzyl alcohol: support effect. Appl. Surf. Sci. 328, 536–547.

Zahmakıran, M., Özkar, S., 2010. The preparation and characterization of gold (0) nanoclusters stabilized by zeolite framework: Highly active, selective and reusable catalyst in aerobic oxidation of benzyl alcohol. Mater. Chem. Phys. 121, 359–363.

Zang, M., Zhao, C., Wang, Y., Chen, S., 2019. A review of recent advances in catalytic combustion of VOCs on perovskite-type catalysts. J. Saudi Chem, Soc.

Zhan, B.-Z., Thompson, A., 2004. Recent developments in the aerobic oxidation of alcohols. Tetrahedron 60, 2917–2935.

Zhan, G., Huang, J., Du, M., Sun, D., Abdul-Rauf, I., Lin, W., Hong, Y., Li, Q., 2012. Liquid phase oxidation of benzyl alcohol to benzaldehyde with novel uncalcined bioreduction Au catalysts: high activity and durability. Chem. Eng. J. 187, 232–238.

Zhang-Steenwinkel, Y., Beckers, J., Bliek, A., 2002. Surface properties and catalytic performance in CO oxidation of cerium substituted lanthanum–manganese oxides. Appl. Catal. A 235, 79–92.

Zheng, W., Liu, R., Peng, D., Meng, G., 2000. Hydrothermal synthesis of $LaFeO_3$ under carbonate-containing medium. Mater. Lett. 43, 19–22.

Zhu, X., Liu, Z., Ming, N., 2010. Perovskite oxide nanotubes: synthesis, structural characterization, properties and applications. J. Mater. Chem. 20, 4015–4030.